

Deadbeat-based control for MMC-HVDC power systems

Majstorović, Milovan; Nougain, Vaibhav; Ristić, Leposava; Lekić, Aleksandra

10.1016/j.ijepes.2025.110583

Publication date

Document Version Final published version

Published in

International Journal of Electrical Power and Energy Systems

Citation (APA)

Majstorović, M., Nougain, V., Ristić, L., & Lekić, A. (2025). Deadbeat-based control for MMC-HVDC power systems. International Journal of Electrical Power and Energy Systems, 167, Article 110583. https://doi.org/10.1016/j.ijepes.2025.110583

Important note

To cite this publication, please use the final published version (if applicable). Please check the document version above.

Other than for strictly personal use, it is not permitted to download, forward or distribute the text or part of it, without the consent of the author(s) and/or copyright holder(s), unless the work is under an open content license such as Creative Commons.

Takedown policy

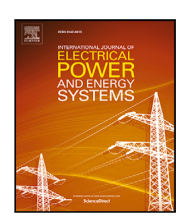
Please contact us and provide details if you believe this document breaches copyrights. We will remove access to the work immediately and investigate your claim.

FISEVIER

Contents lists available at ScienceDirect

International Journal of Electrical Power and Energy Systems

journal homepage: www.elsevier.com/locate/ijepes



Deadbeat-based control for MMC-HVDC power systems[☆]

Milovan Majstorović a^[], Vaibhav Nougain b, Leposava Ristić a^[], Aleksandra Lekić b^[],

- a School of Electrical Engineering, University of Belgrade, Belgrade, Serbia
- b Faculty of Electrical Engineering, Mathematics and Computer Science, Delft University of Technology, Delft, The Netherlands

ARTICLE INFO

Keywords: Modular multilevel converter (MMC) High-voltage direct current (HVDC) transmission Model predictive control (MPC) Deadbeat control

ABSTRACT

With the domination of modular multilevel converters (MMCs) interfaced power grids, especially for transmission of the wind generated energy, the control of such power electronic interfaced grids is of an utmost important for the proper operation and grid stability. This control is very complex due to multivariable intercoupling and plausible nonlinearity. To enhance the grid stability and reduce the total harmonic distortion (THD) of the converter, the paper proposes development of an optimal voltage level-model predictive control (OVL-MPC) for a fast dynamic response, integrated with classical proportional-integral (PI) outer-loop control for robust steady-state performance. This control eliminates the problems of poor steady-state performance of MPC while achieving faster transient response in comparison to the classical proportional integral (PI) dual-loop control. The work proposes OVL-MPC for lower computational burden in comparison to switching state-based MPC, for the inner loop replacing the classical PI inner loop. With the inherent advantages of lower computational burden and superior transient performance, AC current deadbeat controller is used for the modulation in OVL-MPC. To improve the robustness of the control method, the Moore-Penrose pseudo-inversion is applied to address control parameter mismatches, while the Smith predictor compensates for time delays. The designed control algorithm is tested with two real-time simulation platforms, i.e., OPAL-RT and RTDS for thorough power system validation.

1. Introduction

Modular multilevel converters (MMCs) are the most promising converter topology for renewable energy sources integration, offering modularity, scalability, superior power quality, lower switching losses, etc [1]. All of these attributes make MMC-based power systems attractive where the initial system installation cost is not the priority, for e.g., in medium-voltage or high-voltage DC (HVDC) power system applications [2,3]. The high cost of MMCs is derived from huge number (hundreds) of controllable switches being used for better performance, voltage scalability, as well as redundancy and reliability compared with the conventional two-level voltage source converters (VSCs). This means that the control of MMCs is a lot more sophisticated in comparison to the conventional VSCs including, in addition to the primary output power/voltage control, the circulating current and sub-module capacitor voltage balancing control mechanisms [4,5].

The outer loop control objective of a power or voltage control can be realized using linear controllers such as proportional–integral (PI) in transformed rotating dq frame or non-linear controllers like

proportional-resonant (PR) in stationary $\alpha\beta$ frame. The control objective of circulating current and sub-module capacitance voltage balancing are needed to tackle the operation of multiple controllable switches in MMCs. However, these objectives involve multi-variable inter-coupling and strong nonlinearity [6]. If the inner control action can be realized faster using a controller with faster convergence, the outer control action can be subsequently resolved using a conventional linear controller (e.g. PI) making the overall dual-loop control with superior transient performance and robust steady-state performance [7]. Literature has covered a lot of different controllers for power electronic interfaced power grids, such as sliding mode control [8,9], Lyapunovenergy based control [10-12], back-stepping control [13], and others. One such controller with faster convergence and complex multivariable handling attribute is model predictive control (MPC) [7,14-16]. MPC can be useful for defining constraints in complex control problems with relative ease compared to its PI counterpart. It has superior transient performance with the ability to handle complexity, non-linearities and multivariable intercoupling. There are two classes of MPC [17]: (a) switching-state based MPC, (b) voltage-level-based MPC. The authors

E-mail address: majstorovic@etf.bg.ac.rs (M. Majstorović).

¹ Senior Member, IEEE.

This project has received funding from the European Union's HORIZON-WIDERA-2021-ACCESS-03 under grant agreement No. 101079200.

^{*} Corresponding author.

in [6] have covered the classification in detail. The essential difference between the two classes is that in switching-state-based MPC, different possible states of controllable switches are assessed to minimize the defined cost function. This is a computationally burdening method which may lead to the poor steady-state performance. In addition, considerable effort is required to fine-tune the weights for effective cost minimization. Voltage-level-based methods use only N+1 voltage levels (where N is defined as the level of MMC) to find the optimal solution. This reduces an enormous amount of computational burden. However, in comparison to the switching-state based MPC, modulation for MMC switches needs to be done externally in the case of the voltage-level MPCs. Additionally, this can be simplified by using a less detailed MMC averaged model, but it reduces the level of details used for designing control, and thus, it reduces its accuracy [16].

Deadbeat control is one of the best possible solutions to provide a modulation stage without the need to evaluate the weights, cost function, or switching states for the optimal voltage level control [18]. It reduces a lot of computational burden and provides superior transient performance due to faster convergence.

One of the issues of deadbeat control is the influence of time delay in a feedback loop. However, there are several methods to compensate for the time delay, such as the Smith predictor [19], lead compensators [20], or neural network-based system identification, etc. Another issue with deadbeat control is model parameter uncertainties, which can be resolved by applying parameter identification methods, such as Moore–Penrose pseudo-inversion [21], or the implementation of neural networks [22,23] for the parameter identification. Also, these issues and other uncertainties, such as non-linearities of the converter model, can be resolved as shown in [24,25].

Various ac current deadbeat controllers are proposed in the literature for the modulation stage in MMC-based power systems [6,15, 26–29]. These papers utilize the Euler discretization method, which is clear and simple, but less precise compared to the zero-order hold discretization that is used in this paper. Stability analysis considering the influence of parameter mismatch and time delay is conducted in [6], albeit neglecting the active resistance. Furthermore, the circulating current is controlled using a deadbeat controller, which is also the case with [15]. In this paper both circulating and DC input currents are controlled using MPC, relying on its stability and reliability, characteristics needed for the good performances of the MMCs integrated into the HVDC systems.

The proposed work in this paper is focused on exploring the combination of linear outer loop control, optimal voltage level-MPC (OVL-MPC), and classical control for inner loop along with AC deadbeat control for modulation in a multi-terminal MMC-HVDC system. OPAL-RT and RTDS real-time simulations are used to verify the proposed controller to show the validity of the method on different real-time platforms, first on the modulation level with OPAL-RT simulation, and then on the HVDC power system level using RTDS. The performance of the devised controller is tested for different power transients and load switching in the digital twins of TenneT's 2 GW Program [30,31] based on the future plans for European HVDC connection.

The rest of the proposed work is organized as follows. Section 2 dives into the power electronic-building block, i.e., MMC whereas Section 3 analyzes the conventional OVL method and the proposed control method. Section 4 presents the OPAL-RT real-time validation of one MMC device, whereas Section 5 presents the RTDS-based real-time validation to further ensure the plug-and-play control attribute of the proposed control method inside the bigger MMC-based HVDC power system. Finally, Section 6 concludes the work.

2. Modular multilevel converter

The MMC depicted in Fig. 1 has three legs, and each leg consists of two arms. Each arm of the MMC has N_{SM} H-bridge submodules (SMs). The variables shown in Fig. 1 are defined for all three phases, i.e., $j \in$

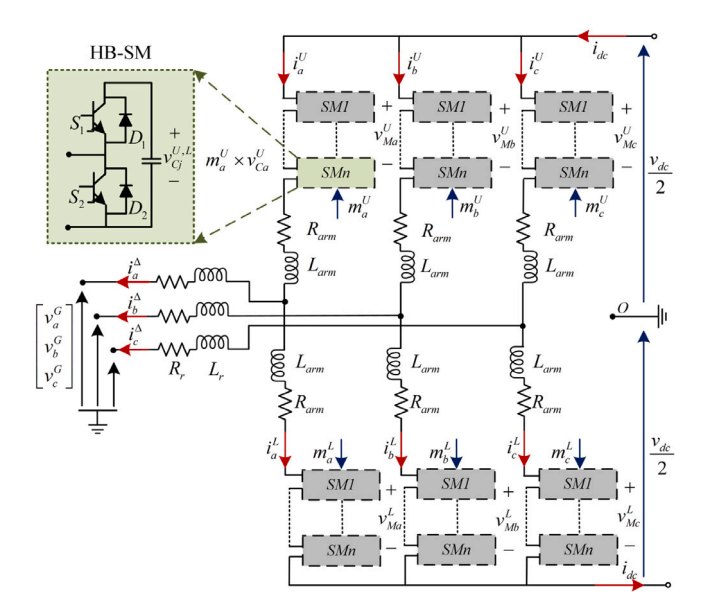


Fig. 1. Three-phase MMC topology.

 $\{a,b,c\}$. Half-bridge SMs are represented by their averaged equivalents, with R_{arm} and L_{arm} being the equivalent arm resistance and inductance, respectively. Each SM has capacitance C_{SM} . The converter model is developed using the $\Sigma-\Delta$ nomenclature, the variables in the upper and lower converter arms can be represented as in [4,6,8,10–12,14,15, 32–34]:

$$i_j^{\Delta} = i_j^U - i_j^L, \quad i_j^{\Sigma} = \frac{i_j^U + i_j^L}{2},$$
 (1a)

$$v_{Mj}^{\Delta} = \frac{-v_{Mj}^{U} + v_{Mj}^{L}}{2}, \quad v_{Mj}^{\Sigma} = v_{Mj}^{U} + v_{Mj}^{L}, \tag{1b}$$

where i_j^U and i_j^L are currents of the upper and the lower arm of the phase $j \in \{a,b,c\}$, while v_{Mj}^U and v_{Mj}^L are the upper and lower arm voltages of the phase $j \in \{a,b,c\}$. DC-bus current is given as

$$i_{dc} = \frac{1}{2} \sum_{j \in \{a,b,c\}} (i_j^U + i_j^L) = \sum_{j \in \{a,b,c\}} i_j^{\Sigma},$$
 (2)

while DC-bus voltage can be expressed as

$$v_{dc} = v_{Mj}^{\Sigma} + 2L_{arm}\frac{\mathrm{d}i_{j}^{\Sigma}}{\mathrm{d}t} + 2R_{arm}i_{j}^{\Sigma}.$$
 (3)

Combining (3) and (2), the dynamic model of DC-bus current is obtained as

$$\frac{di_{dc}}{dt} = \frac{1}{2L_{arm}} \left[3v_{dc} - \sum_{j=a,b,c} v_{Mj}^{\Sigma} - 2R_{arm}i_{dc} \right]. \tag{4}$$

Circulating current of the leg in the phase j is defined with

$$i_{jz} = i_j^{\Sigma} - \frac{i_{dc}}{3}.\tag{5}$$

From (3), (4) and (5), circulating current dynamic model can be presented as

$$\frac{\mathrm{d}\mathbf{i}_{\mathbf{j}\mathbf{z}}}{\mathrm{d}t} = \frac{1}{6L_{arm}} \left[\sum_{j=a,b,c} v_j^{\Sigma} - 3\mathbf{v}_{\mathbf{j}}^{\Sigma} - 6R_{arm}\mathbf{i}_{\mathbf{j}\mathbf{z}} \right],\tag{6}$$

where

$$\mathbf{v}_{\mathbf{j}}^{\Sigma} = \begin{bmatrix} v_{a}^{\Sigma} \\ v_{b}^{\Sigma} \\ v^{\Sigma} \end{bmatrix}, \quad \mathbf{i}_{\mathbf{j}\mathbf{z}} = \begin{bmatrix} i_{az} \\ i_{bz} \\ i_{cz} \end{bmatrix}. \tag{7}$$

Please note that bold symbols in previous equations present vectors, and this notation will be used throughout the text.

From Fig. 1, upper arm voltage can be written as

$$v_{Mj}^{U} = \frac{v_{dc}}{2} - R_{arm}i_{j}^{U} - L_{arm}\frac{\mathrm{d}i_{j}^{U}}{\mathrm{d}t} - Ri_{j}^{\Delta} - L\frac{\mathrm{d}i_{j}^{\Delta}}{\mathrm{d}t} - V_{j}^{G}. \tag{8}$$

Similarly, lower arm voltage is determined by

$$v_{Mj}^{L} = \frac{v_{dc}}{2} - R_{arm} i_j^L - L_{arm} \frac{\operatorname{d}i_j^L}{\operatorname{d}t} + R i_j^\Delta + L \frac{\operatorname{d}i_j^\Delta}{\operatorname{d}t} + V_j^G. \tag{9}$$

With subtraction of (8) from (9), (10) is obtained

$$\begin{split} v_{Mj}^{L} - v_{Mj}^{U} &= R_{arm}(i_{j}^{U} - i_{j}^{L}) + L_{arm} \frac{\mathrm{d}(i_{j}^{U} - i_{j}^{L})}{\mathrm{d}t} \\ &+ 2Ri_{j}^{\Delta} + 2L \frac{\mathrm{d}i_{j}^{\Delta}}{\mathrm{d}t} + 2V_{j}^{G}. \end{split} \tag{10}$$

From combination of (10) with (1a) and (1b) follows

$$2v_{Mj}^{\Delta} = R_{arm}i_j^{\Delta} + L_{arm}\frac{\mathrm{d}i_j^{\Delta}}{\mathrm{d}t} + 2Ri_j^{\Delta} + 2L\frac{\mathrm{d}i_j^{\Delta}}{\mathrm{d}t} + 2V_j^G,$$
(11)

which leads to a dynamic model of the AC currents given as

$$\frac{\mathrm{d}i_j^{\Delta}}{\mathrm{d}t} = \frac{2}{L_{arm} + 2L} \left[v_{Mj}^{\Delta} - v_j^G - \frac{R_{arm} + 2R}{2} i_j^{\Delta} \right]. \tag{12}$$

3. Control method

The control system for an MMC is divided into two sections: the outer control system (OCS) and the inner control system (ICS). The OCS is presented in Fig. 2, and its role is to determine AC and DC current references, which are essential for ICS. OCS is composed of three subsystems: (1) Phase-locked loop (PLL), (2) Active and reactive power control, and (3) Energy control. The first subsystem estimates the phase of the grid voltage. The second one is in charge of determining AC current references necessary to satisfy input variables, active and reactive power reference at the AC terminals $P_{ac,ref}$ and $Q_{ac,ref}$, respectively. The third subsystem produces DC-bus current reference, based on energy stored in SM capacitors using energy-based reference tracking.

3.1. Conventional OVL-MPC

Conventional OVL-MPC [17] is one of the potential solutions for executing the ICS of the MMC. Based on arm current measurements, currents i_j^Σ and i_j^A can be calculated from (1a). The number of the submodules inserted within each leg is constant and set to N_{SM} , i.e. the sum of the number of submodules inserted in the upper arm N_j^U and the lower arm N_j^L equals to $N_j^U + N_j^L = N_{SM}$. This translates to $N_{SM} + 1$ possible combinations of inserted modules in the upper and lower arm. Each pair results in different predicted values for AC and circulating currents, and the pair that offers minimal cost function in each switching period is chosen.

By applying zero-order hold discretization to the dynamic model in Eq. (3), and with $N_j^U=n_j$ and $N_j^L=N_{SM}-n_j$, the predicted value of the current $i_j^{\Sigma,p}$ for the pair $(n_j,N_{SM}-n_j)$ is obtained as

$$\begin{split} i_{j}^{\Sigma,p}[n_{j}] \big((k+1)T_{s} \big) &= i_{j}^{\Sigma}(kT_{s}) e^{\frac{-T_{s}}{\tau_{z}}} \\ &+ \left(v_{dc}(kT_{s}) - V_{Mj}^{\Sigma}[n_{j}](kT_{s}) \right) \frac{1 - e^{\frac{-T_{s}}{\tau_{z}}}}{R_{z}}, \end{split} \tag{13}$$

with $R_z=2R_{arm}$, $L_z=2L_{arm}$, and $\tau_z=L_z/R_z$. Also, v_{dc} and v_{Mj}^{Σ} are considered constant and equal to $V_{dc}(kT_s)$ and $V_{Mj}^{\Sigma}[n_j](kT_s)$, respectively, during the switching period that starts at kT_s , which justifies zero-order hold discretization. Furthermore, value $V_{Mj}^{\Sigma}[n_j](kT_s)$

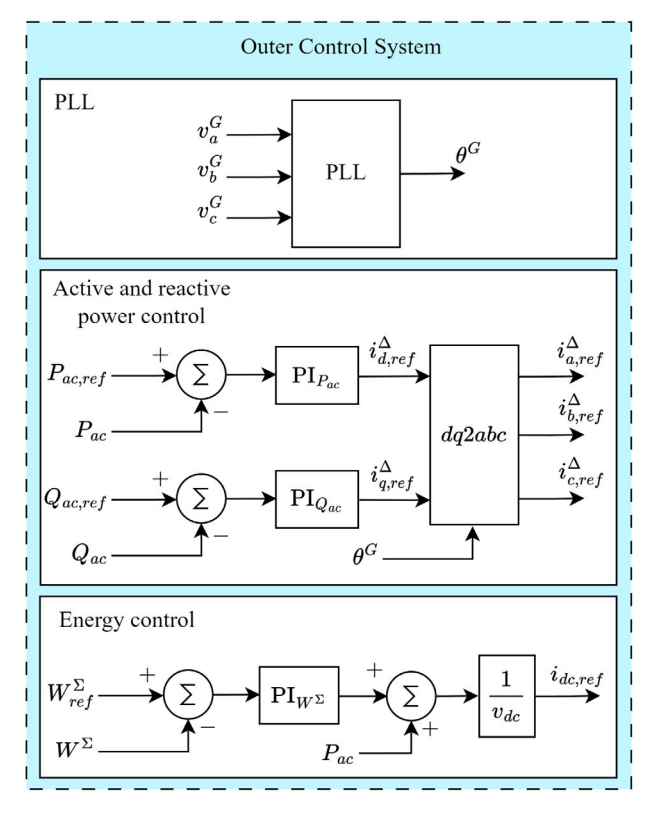


Fig. 2. Block diagram of OCS.

is the function of the number of submodules inserted in the upper arm n_i such as:

$$V_{Mj}^{\Sigma}[n_j](kT_s) = n_j V_{SMj}^{U}(kT_s) + (N_{SM} - n_j) V_{SMj}^{L}(kT_s), \tag{14}$$

where

$$\begin{split} V^{U}_{SMj}(kT_s) &= \frac{1}{N_{SM}} \sum_{x=1,2,...N_{SM}} v^{U}_{SMjx}(kT_s), \\ V^{L}_{SMj}(kT_s) &= \frac{1}{N_{SM}} \sum_{x=1,2,...N_{SM}} v^{L}_{SMjx}(kT_s). \end{split} \tag{15}$$

By applying zero-order hold discretization to Eq. (12), the predicted value of the AC current in phase j for the pair $(n_j, N_{SM} - n_j)$ is obtained as

$$i_{j}^{\Delta,p}[n_{j}]((k+1)T_{s}) = i_{j}^{\Delta}(kT_{s})e^{\frac{-I_{s}}{\tau_{ac}}} + \frac{V_{M_{j}}^{\Delta}[n_{j}](kT_{s}) - V_{j}^{G}(kT_{s})}{R_{ac}} \left(1 - e^{\frac{-T_{s}}{\tau_{ac}}}\right),$$
(16)

with

$$R_{ac} = \frac{R_{arm} + 2R}{2}, \qquad L_{ac} = \frac{L_{arm} + 2L}{2},$$
 (17)

and $\tau_{ac}=L_{ac}/R_{ac}$. Also, $V_{Mj}^{\Delta}[n_j](kT_s)$ and $V_j^G(kT_s)$ are discretized representations of voltages $v_{Mj}^{\Delta}[n_j]$ and v_j^G , respectively, that are considered constant during the switching period that starts at $t=kT_s$. Furthermore, value $V_{Mj}^{\Delta}[n_j](kT_s)$ is the function of the number of submodules inserted in the upper arm n_j and:

$$V_{Mj}^{\Delta}[n_j](kT_s) = \frac{-n_j V_{SMj}^U(kT_s) + (N_{SM} - n_j) V_{SMj}^L(kT_s)}{2}.$$
 (18)

Reference values $i_{j,ref}^{\Delta}$ and $i_{j,ref}^{\Sigma} = i_{dc,ref}/3$ are obtained from OCS. Since OVL-MPC is a per-phase method, each phase has a separate cost

function

$$\operatorname{crit}[n_j] = \lambda^{\Sigma} \left| i_{j,ref}^{\Sigma} \left((k+1)T_s \right) - i^{\Sigma,p} [n_j] \left((k+1)T_s \right) \right|,$$

$$+ \lambda^{\Delta} \left| i_{j,ref}^{\Delta} \left((k+1)T_s \right) - i_{j,p}^{\Delta,p} [n_j] \left((k+1)T_s \right) \right|,$$

$$(19)$$

where λ^{Σ} and λ^{Δ} are weighting factors. Optimal n_j is chosen by minimizing the cost function. Based on the obtained values of n_j , N_j^U and N_i^L are determined for each phase.

3.2. OVL-DB

A block diagram of the ICS of OVL-DB method is presented in Fig. 3. The first block is DC current and circulating currents control, with the role of determining the number of the inserted SMs in the single leg N_j^{Σ} based on DC-bus reference $i_{dc,ref}$, upper and lower arm currents $\mathbf{i}_{\mathbf{j}}^{\mathbf{U}} = [i_a^U, i_b^U, i_c^U]^T$ and $\mathbf{i}_{\mathbf{j}}^{\mathbf{L}} = [i_a^L, i_b^L, i_c^L]^T$, and SM capacitor voltage measurements in both upper and lower arms $\mathbf{v}_{\mathbf{SMjx}}^{\mathbf{U}}$ and $\mathbf{v}_{\mathbf{SMjx}}^{\mathbf{L}}$, respectively. This block can be based on different control mechanisms, and in this paper, OVL-MPC and classical control are used.

As the number of the inserted SMs is fed to the AC current deadbeat control, this block generates not-necessarily integer values $\mathbf{N_j^U} = [N_a^U, N_b^U, N_c^U]^T$ and $\mathbf{N_j^L} = [N_a^L, N_b^L, N_c^L]^T$ to produce good quality of AC current. These values serve as modulation references for both upper and lower arm voltages providing input values for the final block called Balancing and Modulation.

The Balancing and Modulation block also tracks SM capacitor voltages and arm current. The first step is sorting SMs based on their capacitor voltage measurements. Then, sorting results and arm current signs determine whether the individual SM will be inserted, partially inserted, or bypassed, to achieve energy balance throughout the arms. Also, this block keeps the number of the inserted SMs per leg N_j^{Σ} constant throughout the sampling period.

Due to deadbeat and MPC being sensitive to the control parameter mismatch and time delay, Model parameters estimator and Delay compensation blocks are also included in the control structure as can be seen from Fig. 3.

3.2.1. DC-bus and circulating current control

DC-bus and circulating current control are essential for MMC proper operation, so OVL-MPC is one of the possible ways to regulate them. Here, AC current control is excluded from the MPC algorithm, so this block as an output gives the optimal leg voltage level, compared to the usual optimal upper and lower arm voltage levels. The prediction model is based on dynamic models of DC-bus and circulating current models from the previous section.

A zero-order hold discretization method is used in this paper. To utilize this form of the discretization on DC-bus dynamic model from (4), voltages v_{dc} and v_{Mj}^{Σ} are assumed constant and equal to their average values $V_{dc}(kT_s)$ and $v_{Mj}^{\Sigma}(kT_s)$ during one sampling period T_s , with that period starting at kT_s , $k \geq 0$. Then, the DC-bus current predicted value at the next time instant is given as:

$$i_{dc}^{p}((k+1)T_{s}) = i_{dc}(kT_{s})e^{-T_{s}/\tau_{z}} + \left(3V_{dc} - \sum_{j=a,b,c} V_{Mj}^{\Sigma}\right) \frac{1 - e^{-T_{s}/\tau_{z}}}{R_{z}}.$$
(20)

A similar procedure is conducted regarding the circulating current: voltages v_j^{Σ} are considered constant during the individual sampling periods, which justifies zero-order hold discretization. The predicted value of the circulating current i_{jz} at the moment $(k+1)T_s$ based on the measured value of the same current at the moment kT_s , $i_{jz}(kT_s)$, is given as:

$$\mathbf{i}_{\mathbf{j}\mathbf{z}}^{\mathbf{p}}((k+1)T_{s}) = \mathbf{i}_{\mathbf{j}\mathbf{z}}(kT_{s})e^{-T_{s}/\tau_{z}} + \left(\sum_{j=a,b,c} V_{Mj}^{\Sigma} - 3V_{\mathbf{M}\mathbf{j}}^{\Sigma}\right) \frac{1 - e^{-T_{s}/\tau_{z}}}{3R_{z}}.$$
(21)

Voltage V_{Mj}^{Σ} presents leg voltage, and this voltage depends on the SM capacitor voltages throughout the leg and the number of inserted SMs. SM capacitor voltages are not equal one to another, and the number of the inserted SMs between the arms is yet to be determined by the next control block. However, it is assumed that every SM capacitor voltage is equal to the mean value $V_{SMj}(kT_s) = \left(V_{SMj}^U(kT_s) + V_{SMj}^L(kT_s)\right)/2$. So,

$$V_{Mi}^{\Sigma}(kT_s) = N_i^{\Sigma} V_{SMi}(kT_s). \tag{22}$$

Now, it is left to find the optimal value N_j^{Σ} . This number is chosen from the set $n \in \{1, 2, ... 2N\}$. That set is also the domain of the cost function

$$\operatorname{crit}[n] = \lambda_{dc} \left| i_{dc,ref} - i_{dc}^{p} ((k+1)T_{s}) \right|,$$

$$+ \lambda_{z} \sum_{i=a,b,c} \left| i_{jz,ref} - i_{jz}^{p} ((k+1)T_{s}) \right|,$$
(23)

where $i_{dc,ref}$ and λ_{dc} are reference value and weighing factor for DC-bus current, while $i_{jz,ref}$ and λ_z are reference value and weighing factor for circulating currents, respectively. The preferable value of N_z^{Σ} is

$$N_i^{\Sigma} = \operatorname{crit}^{-1} \left[\min \left\{ \operatorname{crit}[n] \right\} \right]. \tag{24}$$

This equation is essential when utilizing OVL-MPC for the DC-bus and circulating current control.

With all three components of the vector $\mathbf{v}_{j,\mathrm{ref}}^{\Sigma}$ in dqz reference frame obtained, it is possible to determine components of the same vector in stationary abc reference frame. Each component in that frame is then divided with the mean value of the SM capacitor voltage for their respective leg, V_{SMj} . Finally, vector \mathbf{N}^{Σ_j} is fed to the next block in the ICS.

Computational burden of OVL in this method is increased from N+1 to 2N+1. However, it is evident that the cost function of the proposed method includes decoupled DC input and circulating currents, unlike the conventional OVL method that regulates i_j^{Σ} separately in each phase.

3.2.2. AC current deadbeat model

The output of the previous block, the number of SMs inserted per leg, N_j^{Σ} , is fed to AC deadbeat current control shown in Fig. 3. Each AC phase has separate deadbeat control. From (16), with replacement of $i_j^{\Delta,p}[n_j] \left((k+1)T_s\right)$ with $i_{j,ref}^{\Delta}(kT_s)$, V_{Mj}^{Δ} can be determined as

$$V_{Mj}^{\Delta} = V_{j}^{G} + \frac{R_{ac} \left(i_{j,ref}^{\Delta}(kT_{s}) - i_{j}^{\Delta}(kT_{s})e^{-T_{s}/\tau_{ac}} \right)}{1 - e^{-T_{s}/\tau_{ac}}}.$$
 (25)

On the other hand,

$$V_{Mj}^{\Delta} = \frac{N_j^L(kT_s)V_{SMj}^L(kT_s) - N_j^U(kT_s)V_{SMj}^U(kT_s)}{2},$$
(26)

where $N_j^U(kT_s)$ and $N_j^L(kT_s)$ are the number of SMs that will be inserted in the upper and lower arm of the phase j for the following sample period T_s .

Taking into account relation $N_j^L = N_j^\Sigma - N_j^U$ with (25) and (26), the number of the SMs that need to be inserted in the upper arm of the phase j can be calculated from

$$N_{j}^{U} = \frac{N_{j}^{\Sigma} V_{SMj}^{L} - 2V_{j}^{G} - \frac{2R_{ac} \left(i_{j,ref}^{\Delta}(kT_{s}) - i_{j}^{\Delta}(kT_{s})e^{-T_{s}/\tau_{ac}} \right)}{1 - e^{-T_{s}/\tau_{ac}}}}{V_{SMj}^{U} + V_{SMj}^{L}}.$$
(27)

So, the main idea of the proposed method is to utilize non-integer values for N_j^U and N_j^L (the number of SMs inserted in the lower arm), while still maintaining their sum to be N_j^Σ throughout the switching period. This is accomplished by simultaneously changing the integer values of N_j^U and N_j^L with help from the two modulation carriers, each for each arm of the single phase.

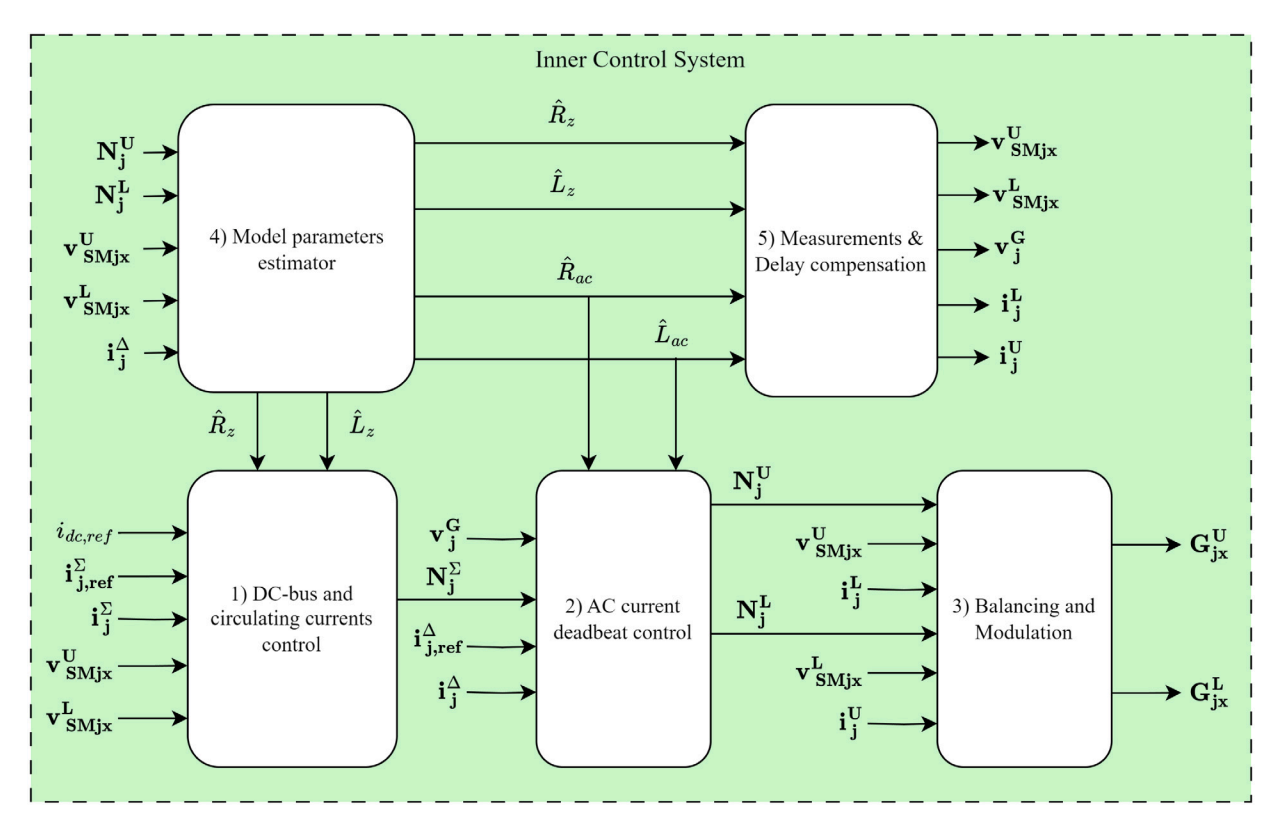


Fig. 3. Block diagram of ICS with utilization of OVL-DB.

3.2.3. Modulation

The deadbeat algorithm determines N_j^U and N_j^L for each phase, and these values are forwarded to the modulation block. The modulation block has a balancing algorithm incorporated; the number of SMs inserted in upper arm throughout the whole switching period is equal to the floor of the non-integer number N_j^U (references of these SMs are set to one), while the number of SMs bypassed in the same arm is equal to $N-\lceil N_j^U \rceil$ (their references are set to zero). There is a single SM remaining, and reference of this SM is assigned to $N-\lfloor N_j^U \rfloor$. Thanks to this reference, a non-integer average number of inserted SMs throughout the switching period is achieved. The choice of which SMs will be inserted, bypassed, or partially inserted (SM with non-integer reference value) is made based on the sign of the arm current and SM voltages, to achieve balanced energy distribution throughout the arm. The modulation principle is presented in Fig. 4.

3.2.4. Model parameters estimator

An error in control parameters can affect the performance of any control system, but it has an even greater impact on control algorithms that rely heavily on the parameter values, such as deadbeat control. The influence of parameter discrepancy on algorithm performance is analyzed in the following text and a parameter estimation procedure is proposed to overcome this issue.

Block diagram of the deadbeat control accounting for model parameter mismatch and the time delay is given in Fig. 5. In this part of the analysis, the time delay is neglected, i.e., a=0. Now, the closed-loop transfer function is:

$$G_{CL}(z) = \frac{\frac{k_R R_{ac}}{1 - E_c} \frac{1}{R_{ac}} \frac{1 - E}{z - E}}{1 + \frac{k_R R_{ac}}{1 - E_c} \frac{1}{R_{ac}} \frac{1 - E}{z - E} E_c},$$
(28)

where $k_R = R_{ac,c}/R_{ac}$ is the mismatch coefficient of the AC load resistance, and

$$E = e^{\frac{-T_s R_{ac}}{Lac}}, E_c = e^{\frac{-T_s R_{ac,c}}{L_{ac,c}}} = e^{\frac{-T_s R_{Rac}}{k_L L_{ac}}},$$
(29)

where $k_L = L_{ac,c}/L_{ac}$ is the mismatch coefficient of the AC load inductance. With the substitution $\gamma = k_R/k_L$ in Eq. (28), it becomes:

$$G_{CL}(z) = \frac{\frac{k_R R_{ac}}{1 - E^{\gamma}} \frac{1 - E}{R_{ac}}}{1 + \frac{k_R R_{ac}}{1 - E^{\gamma}} \frac{1 - E}{R_{ac}} \frac{1 - E}{z - E}}.$$
(30)

For further simplification, (30) can be rewritten as

$$G_{CL}(z) = \frac{k_R(1-E)}{z(1-E^{\gamma}) - E(1-E^{\gamma}) + k_R E^{\gamma}(1-E)}. \tag{31} \label{eq:GL}$$

So, the single pole of transfer function (31) equals

$$z_p = \frac{E(1 - E^{\gamma}) - k_R E^{\gamma} (1 - E)}{1 - E^{\gamma}} = E - \frac{k_R E^{\gamma} (1 - E)}{1 - E^{\gamma}}.$$
 (32)

The system is stable provided that

$$-1 \le z_p \le 1,\tag{33}$$

i.e.,

$$-1 \le E - \frac{k_R E^{\gamma} (1 - E)}{1 - E^{\gamma}} \le 1. \tag{34}$$

The second part of (34) is satisfied as both minuend and subtrahend being positive, and $E \leq 1$. Regarding the second part of the condition $(z_p \geq -1)$, numerical analysis reveals values of k_R and k_L for which this condition is violated, which leads to system instability. For example, for $k_R, k_L \in (1/3, 3)$, there are cases where z_p is smaller that -1. However, for $k_R, k_L \in (1/2, 2)$ there are no such instances.

The previous analysis shows that unchecked parameter variations may lead to system instability. To ensure system stability, it is necessary to conduct model parameter estimation during system operation. In this paper, the Moore–Penrose inverse application will be used to determine parameter values for pairs (R_z, L_z) and (R_{ac}, L_{ac}) . This approach is particularly useful when the number of parameters involved is relatively low and a large number of sampling points is available. Such problems can generally be formulated as

$$b_k = x_1 a_{1k} + x_2 a_{2k} + \dots + x_M a_{Mk}, \quad k \in \{1, 2, \dots, N\},$$
 (35)

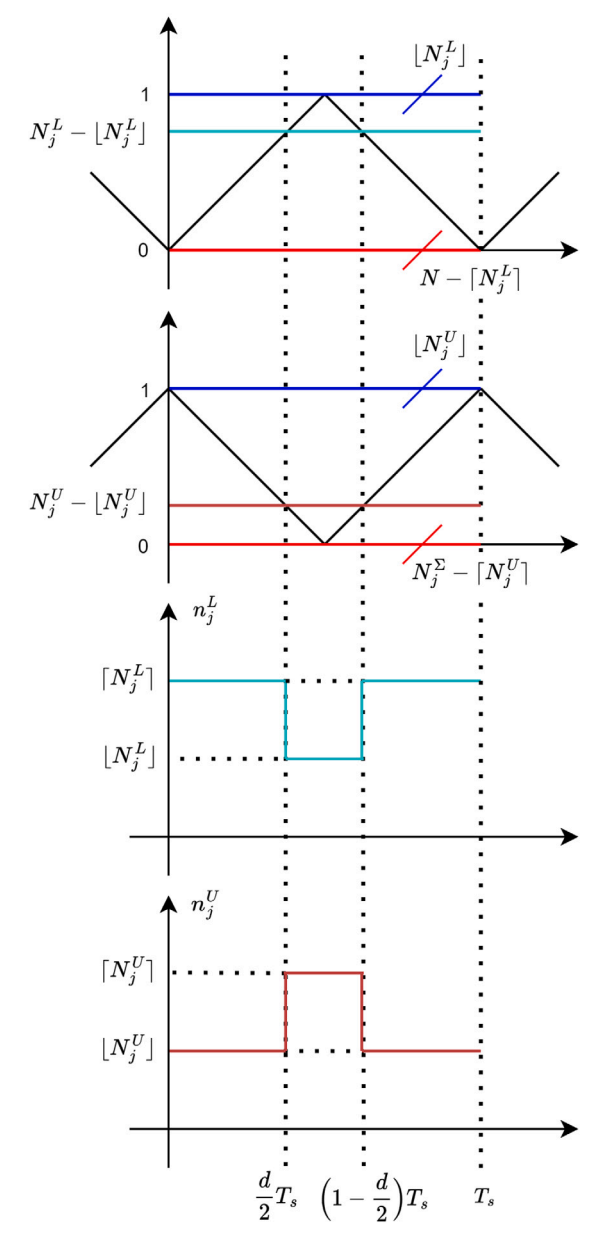


Fig. 4. Modulation principle of OVL-DB method.

where k is the sample number, b_k is the kth output sample, a_{jk} ($j \in \{1,2,\ldots,M\}$) is the kth sample of the jth input quantity, and x_j is the jth parameter value. The total number of samples is N and the total number of parameters and input quantities is M. Eq. (35) can be formulated in matrix form as

$$\mathbf{b} = \mathbf{A}\mathbf{x},\tag{36}$$

where $\mathbf{b}_{N\times 1}$ is the output vector, $\mathbf{A}_{N\times M}$ is the input matrix, and $\mathbf{x}_{M\times 1}$ is the parameter vector. The elements of the input and output matrices are considered known (measured quantities), and the parameter values are to be determined. As $N\neq M$ in general, the input matrix is not square and matrix inversion is not applicable. However, the parameter vector can be determined by applying the Moore–Penrose inverse, i.e., the pseudoinverse, as follows

$$\mathbf{x} = (\mathbf{A}^{\mathsf{T}} \mathbf{A})^{-1} \mathbf{A}^{\mathsf{T}} \mathbf{b} = \mathbf{A}^{+} \mathbf{b}, \tag{37}$$

where $A^+ \equiv (A^T A)^{-1} A^T$ is the pseudoinverse of matrix A. Note that the dimensions of the matrix product $A^T A$ being inverted are $M \times M$.

When the number of parameters M is low, the inversion procedure is computationally simple, which is particularly convenient for real-time parameter estimation. The parameter values obtained using this procedure guarantee a minimal sum of squared errors between the measured and calculated output values.

For an RL load, the current in the next sampling instant can be calculated based on the current in the observed sampling instant and the applied voltage as

$$i_{k+1} = i_k \cdot e^{-\frac{\Delta t}{\tau}} + \frac{v_k}{R} \left(1 - e^{-\frac{\Delta t}{\tau}} \right)$$

$$\approx i_k \left(1 - \frac{\Delta t}{\tau} \right) + \frac{v_k}{R} \frac{\Delta t}{\tau},$$
(38)

where i_k and i_{k+1} are current measurements at the time instants $k\Delta t$ and $(k+1)\Delta t$, respectively, while v_k is voltage distributed across the resistor and inductor. Since the voltage of the converter is changing during the switching period, it is preferable to set Δt significantly smaller than T_s , which can also be helpful for the approximation in previous equation. The previous formulation is suitable for a single-phase load; a slight modification is required for a three-phase system. Namely, the reference voltages may contain a zero-sequence component

$$v_0 = \frac{v_a + v_b + v_c}{3},\tag{39}$$

which needs to be subtracted from each phase voltage. By doing so, phase currents are obtained as follows

$$\begin{split} i_{a,k+1} &\approx i_{a,k} \left(1 - \frac{\Delta t}{\tau} \right) + \frac{2}{3} \frac{\upsilon_{a,k} - \frac{1}{2} \upsilon_{b,k} - \frac{1}{2} \upsilon_{c,k}}{R} \frac{\Delta t}{\tau} \\ &= i_{a,k} \left(1 - \frac{\Delta t}{\tau} \right) + \frac{\upsilon_{a0,k}}{R} \frac{\Delta t}{\tau}, \\ i_{b,k+1} &\approx i_{b,k} \left(1 - \frac{\Delta t}{\tau} \right) + \frac{2}{3} \frac{\upsilon_{b,k} - \frac{1}{2} \upsilon_{c,k} - \frac{1}{2} \upsilon_{a,k}}{R} \frac{\Delta t}{\tau} \\ &= i_{b,k} \left(1 - \frac{\Delta t}{\tau} \right) + \frac{\upsilon_{b0,k}}{R} \frac{\Delta t}{\tau}, \\ i_{c,k+1} &\approx i_{c,k} \left(1 - \frac{\Delta t}{\tau} \right) + \frac{2}{3} \frac{\upsilon_{c,k} - \frac{1}{2} \upsilon_{a,k} - \frac{1}{2} \upsilon_{b,k}}{R} \frac{\Delta t}{\tau} \\ &= i_{c,k} \left(1 - \frac{\Delta t}{\tau} \right) + \frac{\upsilon_{c0,k}}{R} \frac{\Delta t}{\tau}. \end{split}$$

$$(40)$$

The previous equations can be expressed in terms of measured quantities and unknown parameters:

$$i_{j,k+1} = i_{j,k} x_1 + v_{j0,k} x_2, (41)$$

where *j* denotes one of the three phases and

$$x_1 = 1 - \frac{\Delta t}{\tau}, \quad x_2 = \frac{\Delta t}{\tau R}.$$
 (42)

Note that the form of (41) corresponds to (35), wherein:

$$i_{j,k+1} \to b_k, \quad i_{j,k} \to a_{1k}, \quad v_{j0,k} \to a_{2k}.$$
 (43)

A matrix formulation corresponding to (36) now can be obtained. The parameters vector \mathbf{x} can now be obtained from (37). After determining the values of x_1 and x_2 , the load parameters are calculated as:

$$L = \frac{\Delta t}{x_2}, \quad R = \frac{L}{\Delta t}(1 - x_1). \tag{44}$$

3.2.5. Delay compensation

In this analysis it is assumed that the actual model parameters are obtained by the estimation procedure, so k_L and k_R are equal to 1 and also $E_c=E$. Therefore, the closed-loop transfer function of the system from Fig. 5 becomes

$$G_{CL}(z) = \frac{\frac{R_{ac}}{1-E} \frac{1}{R_{ac}} \frac{1-E}{z-E}}{1 + \frac{R_{ac}}{1-E} \frac{1}{R_{ac}} \frac{1-E}{z-E} E \cdot z^{-a}},$$
(45)

which can be further simplified to

$$G_{CL}(z) = \frac{1}{z + E \cdot z^{-a} - E}. (46)$$

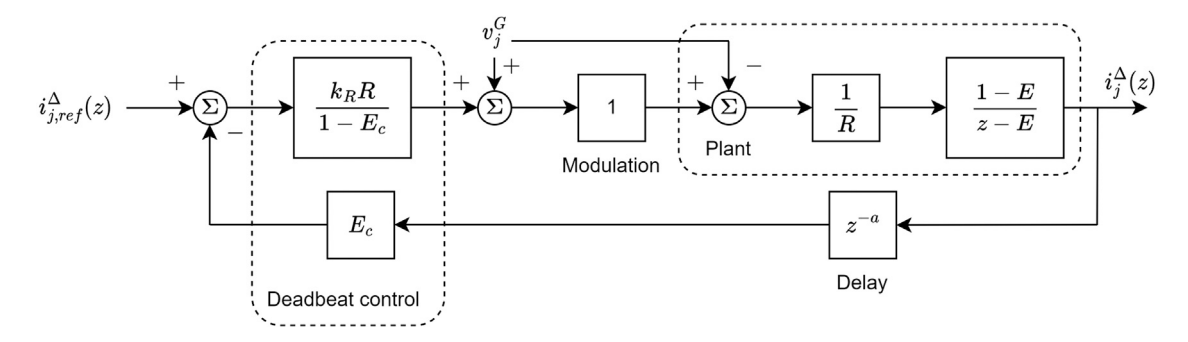


Fig. 5. Block diagram of deadbeat control with false model parameters and the time delay.

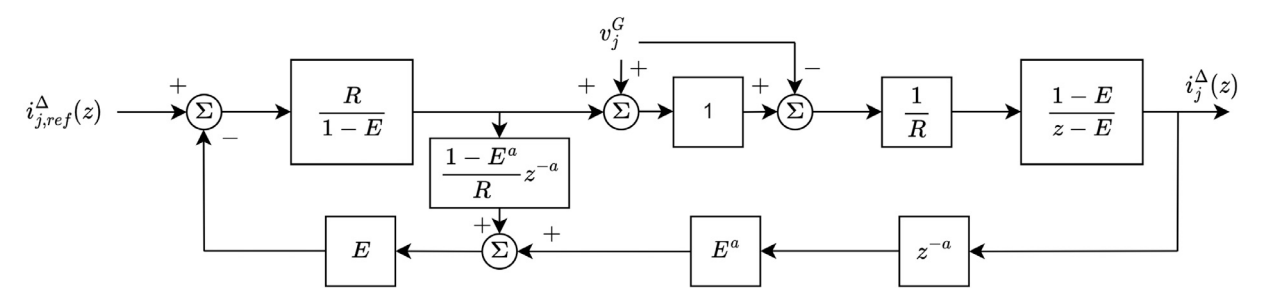


Fig. 6. Block diagram of deadbeat control with Smith predictor.

When a = 1, which corresponds to a unit delay, the poles of the transfer function (46) are

$$z_{p1,2} = \frac{E \pm \sqrt{E^2 - 4E}}{2}. (47)$$

The module of these poles is equal to

$$|z_{p1,2}| = \sqrt{E},$$
 (48)

which means that when $E \rightarrow 1$ ($\tau_{ac} \gg T_s$), system stability is compromised.

To insure system stability when a time delay is present, delay compensation is required. Delay compensation is based on measurements, former control inputs, and estimated model parameters. In this paper, a Smith predictor is used, as shown in Fig. 6. Closed-loop transfer function of this system is

$$G_{CL}(z) = (1 - E)/$$

$$(z(1 - E) - E + E^2 + z^{1-a}(E - E^{a+1}) - z^{-a}(E^2 - E^{a+1})).$$
(49)

When a = 1, the transfer function becomes 1/z, i.e., the pole is relocated to 0, and hence system stability is not longer compromised.

4. OPAL-RT verification of standalone MMC with the passive load

In this section, the control algorithm that utilizes OVL-MPC as a DC-bus and circulating current controller is implemented with the topology from Fig. 1. MMC is connected to the constant DC source on the DC terminal, while on AC terminals, RL three-phase load is connected. MMC parameters are: DC source voltage $v_{dc}=100$ V, number of SMs within the single arm N=4, switching frequency $f_s=4$ kHz ($T_s=250~\mu \rm s$), arm inductance $L_{arm}=4$ mH, arm resistance $R_{arm}=10$ m Ω , SM capacitance $C_{sm}=10$ mF. Load parameters are the resistance of $R=10~\Omega$ and inductance of L=10 mH. There is no three-phase grid present in this simulation, meaning grid voltage v_j^G is equal to the zero for every $j\in\{a,b,c\}$, with a passive load connected in the Y configuration. Since there is no grid voltage, AC current reference frequency is equal to f=50 Hz, and angle of the AC current reference is equal to $\theta^G=2\pi ft$. Also, in this simulation, only active power is being controlled, while $i_{q,ref}^A$, the output of the reactive power controller, is set to zero.

The idea of this section is to test the control algorithm with passive load, and also with a small number of SMs. MMC topologies with a small number of SMs are topologies where a significant improvement in AC current quality is expected when using this control algorithm, as compared to the classical OVL-MPC control mechanism. First, this amplitude of AC current reference value is set to $I^* = 2.5$ A. Then, at time instant 0.05 s, this value is suddenly changed to the 4 A.

From Fig. 7 can be concluded that AC current responses successfully track their respective references even with the sudden changes in the reference amplitude. In a range of several switching periods, responses were able to retain a trajectory similar to the references. The DC-bus current and circulating current achieve a steady-state around 10 ms after a sudden change has occurred.

Time diagrams of the newly achieved steady-state are presented in Figs. 8 and 9. As can be seen, AC current responses are fair shadows of the AC current references, with their THD factor being equal to 1.25%. THD of the AC current response for the different reference amplitude when using conventional OVL-MPC and OVL-DB, are presented in Fig. 10. There is a significant improvement in the THD factor when using OVL-DB compared to conventional OVL for all AC current amplitude values. Furthermore, DC-bus current i_{dc} and circulating currents i_{az} , i_{bz} and i_{cz} are larger together with the larger AC current amplitudes. The AC component of the DC-bus current is insignificant compared to the DC component. A major component of the circulating currents is at double the fundamental frequency $2f=100~{\rm Hz}$, forming an inverting-sequence three-phase current system, with amplitude kept under 0.2 A.

SM voltages of the phase a are presented in Fig. 9. The well-balanced nature of the SM voltages within the arms is presented in the first two time diagrams. The differences between SM voltages when appearing are quickly diminished. The third diagram is proof of good arm energy balancing within a single leg, with average values of Σv_{aux} and Σv_{alx} being 99.8 V and 99.5 V, respectively.

Circuit parameters can change over time (temperature effects, aging, inductor saturation, etc.) or not be properly identified to begin with. The proposed control method is tested with faulty control parameters to verify its robustness to such discrepancies, both in steady-state and transient.

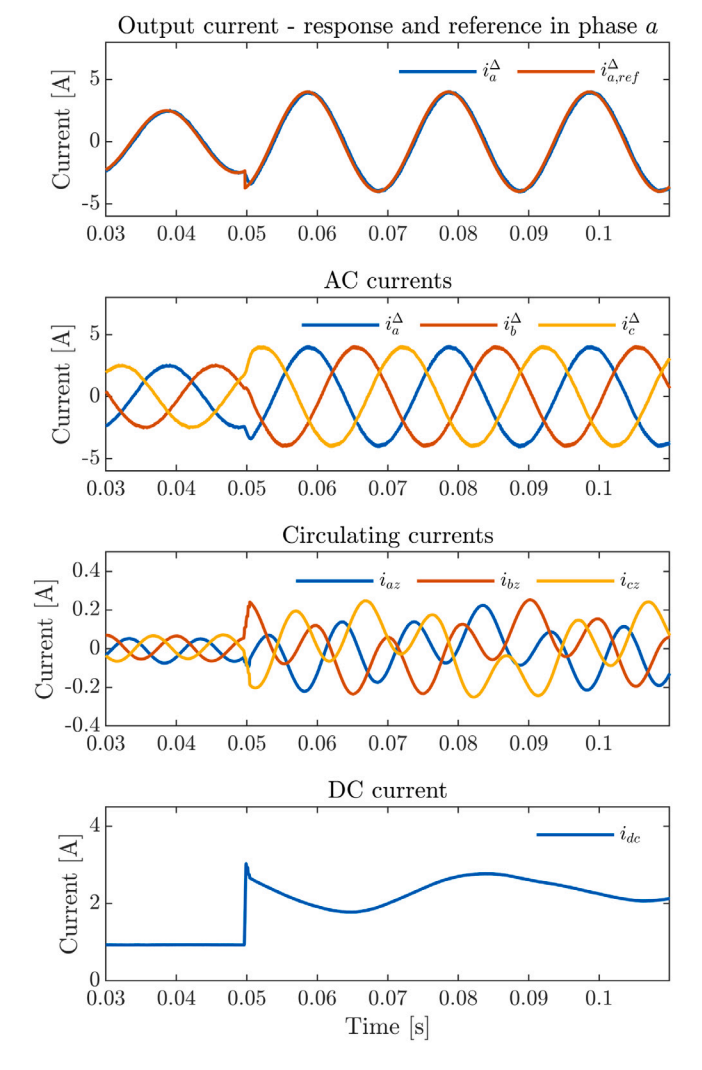


Fig. 7. Time diagrams of AC, circulating, and DC current during transient - RL load.

Fig. 11 represents the simulation results when load resistance R is changed from 10 Ω to 15 Ω , while maintaining that control parameter at $R_c=10~\Omega$. The control inductance is $L_c=10~\mathrm{mH}$, which corresponds to the actual AC load inductance value. At $t=1~\mathrm{s}$, the active power reference is stepped up from 75 W to 150 W. Before and after the change, the amplitude of AC current response is smaller by around 11% than the amplitude of the reference. In the simulation with correct control parameters, the current response amplitude is around 11 % larger than the current reference amplitude with the faulty R_c (1.5 times smaller than the actual value $R=15~\Omega$). This mismatch is due to AC power controller in OCS, i.e., power invariance ($\sqrt{1.5}-1\approx0.22$). Due to this, the amplitude of the AC current reference in simulation with the faulty parameters is exactly in between the response amplitude with the faulty parameters and the response amplitude with the correct parameters.

Fig. 12 represents the simulation results when load inductance is changed from 10 mH to 30 mH, while maintaining control inductance at $L_c=10$ mH. The resistance $R_c=10~\Omega$, which corresponds to the actual AC load resistance value. Again, at $t=1~\rm s$, the active power reference is changed from 75 W to 150 W. The amplitude of the AC current response is lower than the amplitude of the AC current reference by less than 3 %. Additionally, due to the parameter mismatch, AC current response lags the AC current reference by 410 μs , which corresponds to a phase shift of 7.38° angle.

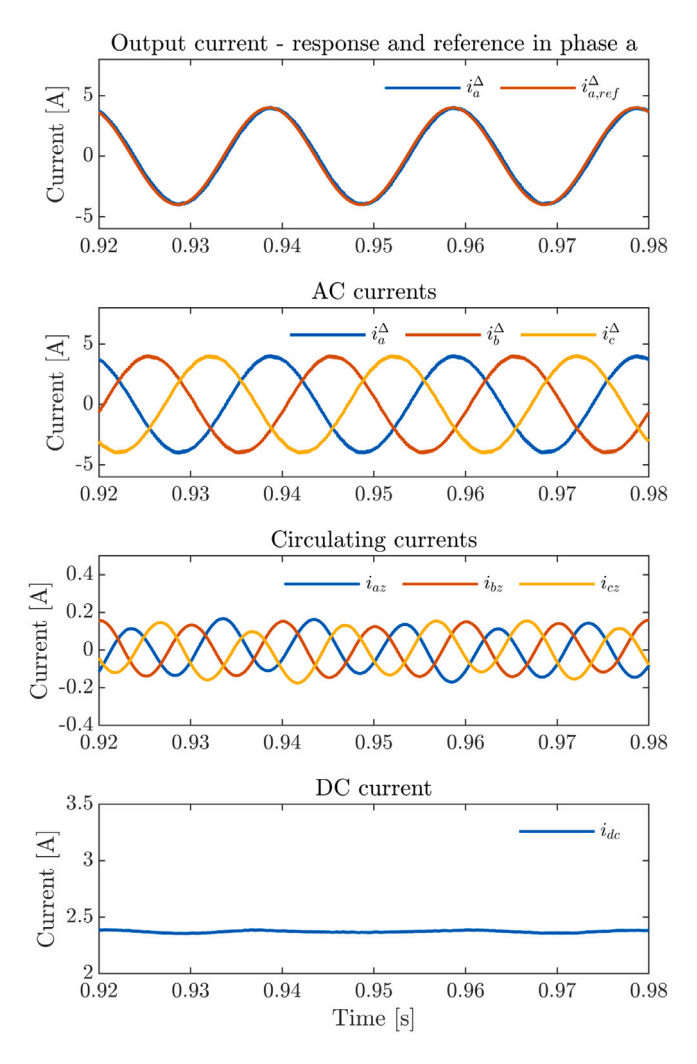


Fig. 8. Time diagrams of AC, circulating, and DC current during steady-state - RL load.

In both of the analyzed cases there is a noticeable deviation between the current response and the reference current. However, the system remains stable and the AC power response is in accordance with the reference.

The simulation results provided so far are obtained without employing the model parameter estimator. Fig. 13 demonstrates the transition of AC current reference and response upon engaging the estimator. The AC load parameters written in the control $R_c=10~\Omega$ and $L_c=10~\mathrm{mH}$, whereas the actual AC load resistance and inductance are $R=8~\Omega$ and 15 mH. The estimator is turned on at the $t=0.5~\mathrm{s}$. Before engaging the estimator, the current response had a higher amplitude and was lagging behind the current reference. After including the estimator, the deviation of the current response is quickly eliminated and the response proceeds to follow the reference without notable error.

5. RTDS verification of MMC-based HVDC power system

Since a single OPAL-RT could not support detailed real-time simulation of the larger HVDC power system, an additional RTDS-based simulation has been performed using an RTDS NovaCor rack with 7 cores. The incorporated RTDS setup for the multi-terminal HVDC power system is explained in [7,30], together with the control principles. The multi-terminal MMC-based HVDC power system simulated for this work, depicted in Fig. 14, consists of an offshore wind-connected grid-forming converter MMC2 connected to the conventional grid via

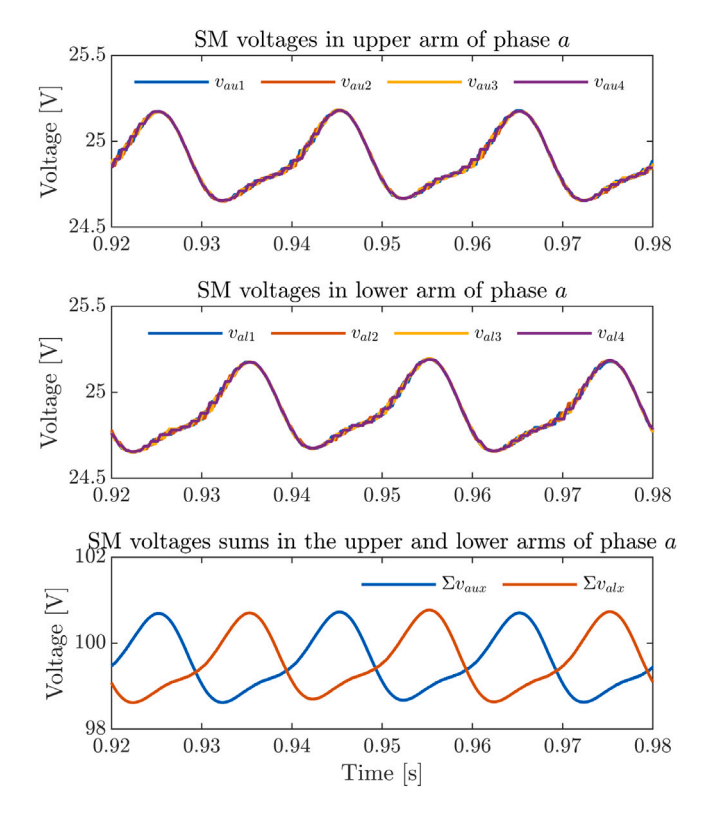


Fig. 9. Time diagrams of SM voltages in the phase a during steady-state - RL load.

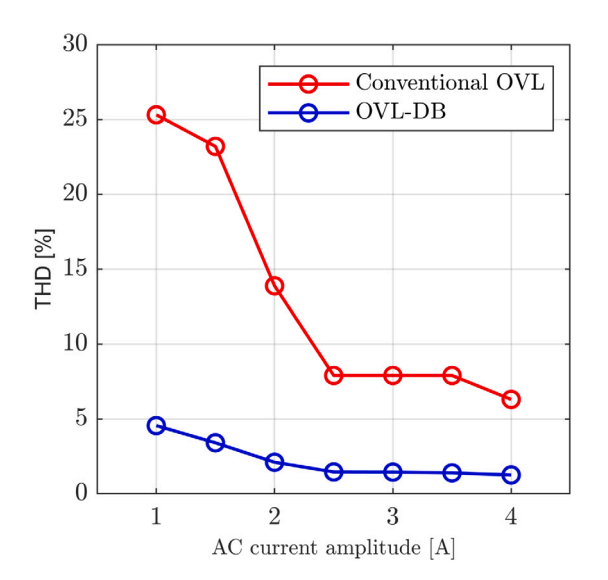


Fig. 10. THD factor of AC currents when using the conventional OVL vs. OVL-DB depending on the AC current amplitude.

long underground cables and grid-following converters MMC1 and MMC3. For the simulation using real-time RTDS setup, the bipolar configuration of each terminal is taken into account. Upper MMC is on its DC side connected between the positive and neutral terminal of the HVDC, while lower MMC is connected between the neutral and negative terminal of the HVDC. The nominal voltage of the HVDC is ± 525 kV. On the AC side, each MMC is connected via a separate three-phase transformer (1350 MVA, 275 kV/400 kV, D/Yn) to the AC grid 3×400 kV, 50 Hz. Transformer leakage reactance is equal to 0.18 p.u. Regarding the MMCs, the number of SMs per arm is N=200, arm inductance equals $L_{arm}=39.7$ mH, and SM capacitance is $C_{sm}=15$ mF.

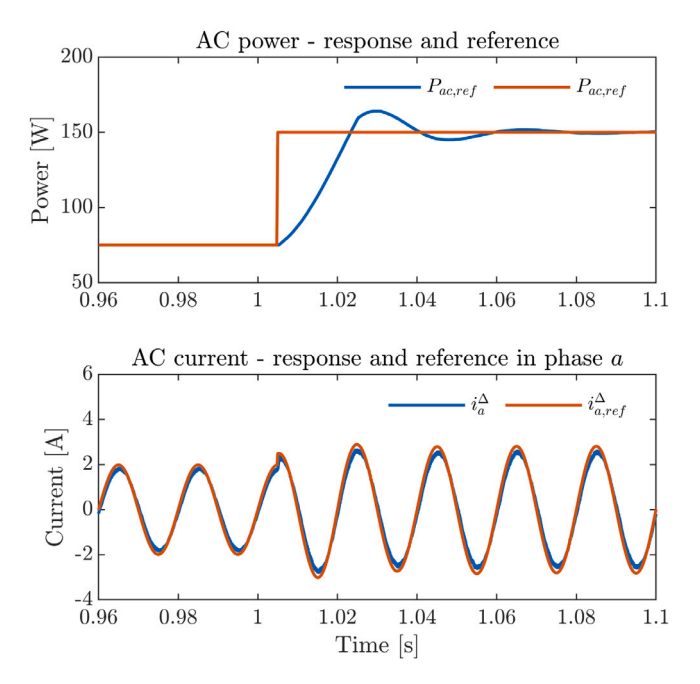


Fig. 11. False parameters: power and AC current reference and response while R=15 Ω and $R_{c}=10$ Ω .

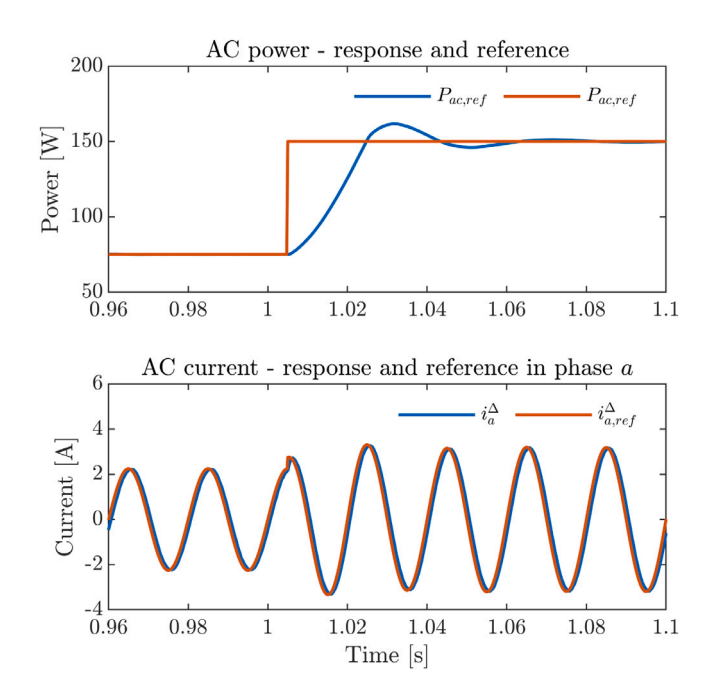


Fig. 12. False parameters: power and AC current reference and response while $L=30\,$ mH and $L_c=10\,$ mH.

The period of the carrier used in the modulation, also being the sample time of the control, is at $T_s=500~\mu s$ ($f_s=2~kHz$). Converters MMC1 and MM2 have standard PI control implementations as explained in [30], and MMC3 control is modified to the proposed OVL-DB.

While designing the controls, the parameters were chosen in order that would respect the grid codes pre-defined for the future HVDC European grid, and performed small disturbance test cases such as power reference step change. For these test cases, as the crucial test is observed the smooth tracking of the reference values, i.e. without overshoots which for the HVDC power system can go between $\pm 5\%$ of the nominal/desired value.

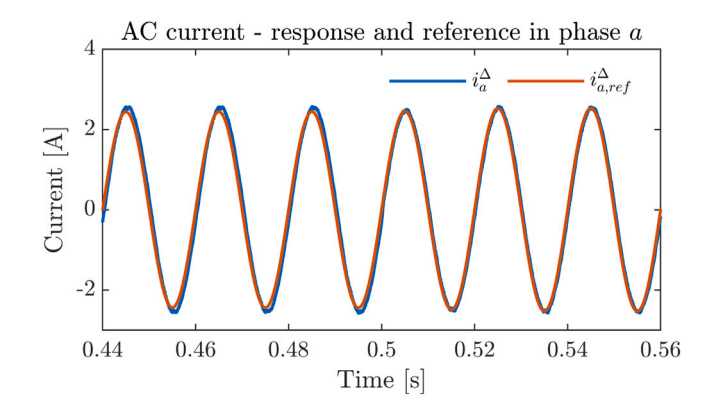


Fig. 13. False parameters: AC current reference and response while turning on the model parameters estimator.

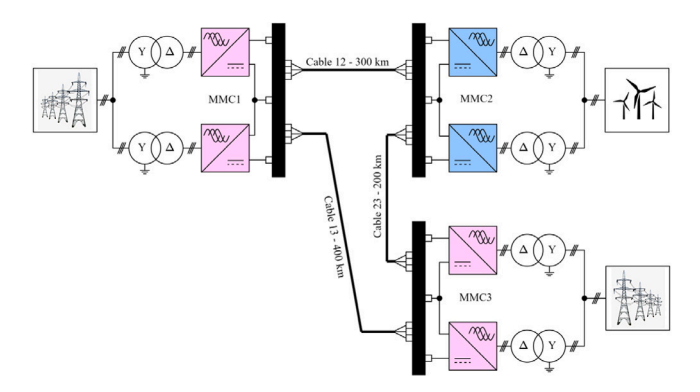


Fig. 14. Three terminal MMC-based HVDC power system simulated in RTDS.

Fig. 15 presents transient results of MMC3 after operational (active and reactive power) reference step change. At the time instant of t = 1 s, the active power reference is changed from 500 MW to 1000 MW, while the reactive power reference is at 0. The figure contains time diagrams of active and reactive power at the references at the transformer's AC grid side and responses, the AC currents at the same place, and the DC-bus currents at the positive and negative terminal of the HVDC. Reactive power reference and response are at zero during the transient period, with response closely following reference. Active power response is at reference value again after 0.065 s after the change. This is due to increased time constant of active and reactive power control in the outer control loop, to ensure a smoother response and improve the system's stability. The AC current amplitude progressively increases during the same 0.065 time interval. AC currents form a direct-sequence three-phase system with their amplitude progressively changing from 1.53 kA to 2.96 kA. Circulating currents form an inversesequence three-phase system with double the fundamental frequency, i.e., 2f = 100 Hz. During the transient, the amplitude of the circulating currents steadily reaches 0.34 kA, starting from 0.166 kA before the power reference change. The positive terminal DC-bus current of the single MMC jumps from 2.45 kA to 5 kA with a time interval of 0.12 s needed to achieve a new steady-state compared to the first two time diagrams. The behavior of the negative terminal DC-bus current is similar to the positive terminal current, with the only difference being with the sign of current. Overall, from Fig. 15 can be observed a good tracking of active and reactive power and fast reaction to the disturbance.

Furthermore, at the new steady-state (Fig. 16), active and reactive power response overlaps with the corresponding references at 1000 MW and 0 MVAr. The power responses align closely with their respective reference values, demonstrating stable steady-state performance.

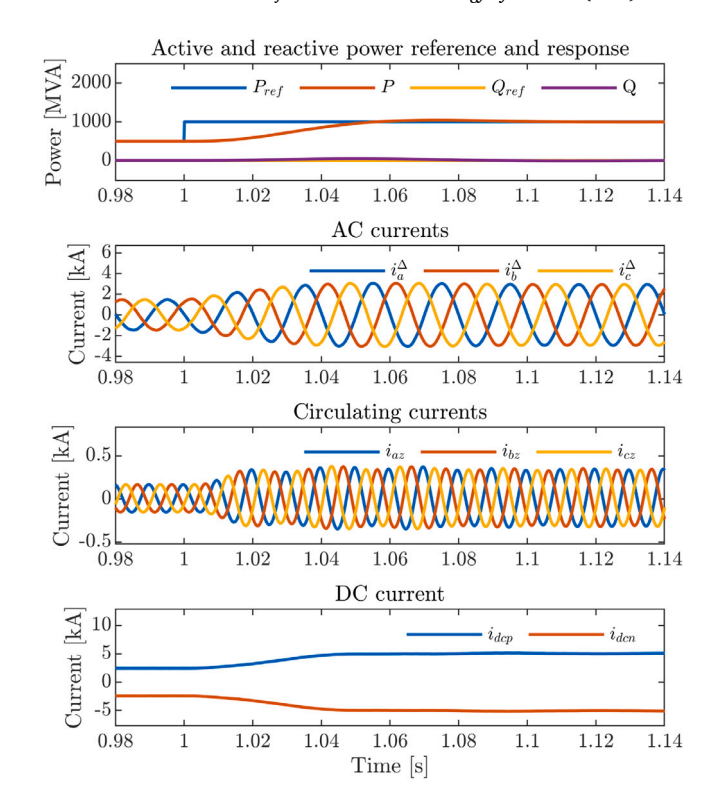


Fig. 15. MMC3's time diagrams during transient: active power reference change from 500 MW to 1000 MW.

Table 1
THD factor vs. active power reference.

The factor vs. active power reference.	
P_{ref} [MW]	THD [%]
-1000	1.3
-750	1.35
-500	1.84
-250	2.88
250	3.12
500	1.89
750	1.31
1000	1.29

The AC currents form direct-sequence system at 50 Hz. The THD factor of the AC currents over the interval from 1.92 s to 1.98 s equals 1.28%. DC-bus current is relatively constant, with switching harmonics present starting from $f_s=2\,$ kHz. Circulating currents contain second-order harmonics at 100 Hz, and together forms inverse-sequence three-phase system. Circulating current amplitude are around 10% of AC current amplitude.

Additional change of the reference happens at time instant t=2 s, where active power reference is changed back to 500 MW from 1000 MW. Similar to the first test, a new steady-state is achieved after 0.065 s, with AC, circulating, and DC-bus currents back at their original amplitude values before the 1 s time instant. The system remain stable after returning to its original state. This is depicted in Fig. 17.

As it can be concluded, the proposed control approach is interoperable in the bigger three-terminal HVDC power system and confirms the conclusions of the stable control operation for a standalone MMC, provided by OPAL-RT simulation. Furthermore, THD factor values for different active power references are presented in Table 1. In accordance to the THD value definition, MMC3's AC current quality is better with the greater active power reference values, in both cases: when active power is taken from the AC grid (negative values of P_{ref}), and active power is supplied to the AC grid (positive values of P_{ref}).

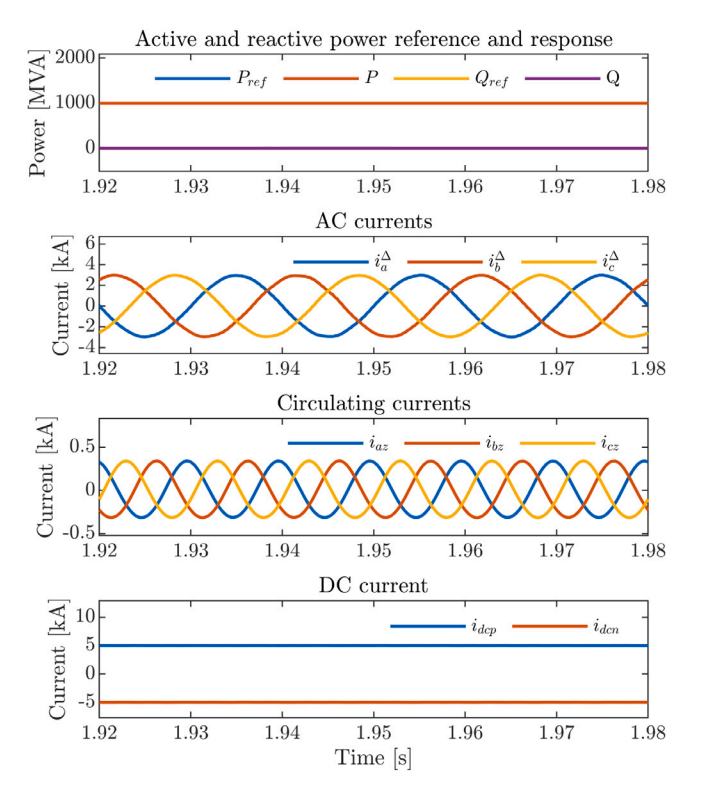


Fig. 16. MMC3's time diagrams during steady-state: active power reference at $1000 \, \text{MW}$

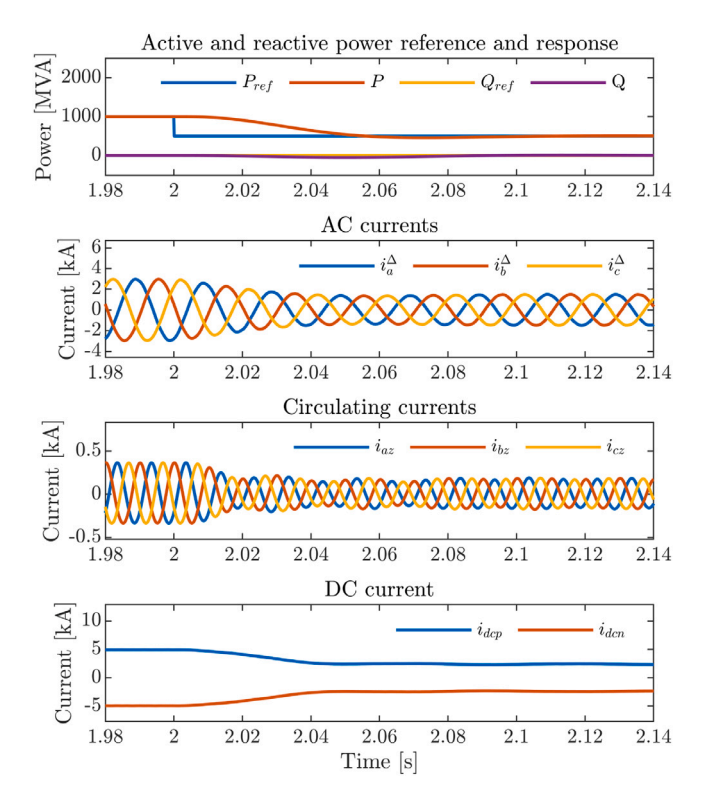


Fig. 17. MMC3's time diagrams during transient: active power reference change from $1000\ MW$ to $500\ MW$.

6. Conclusion

This work develops an optimal voltage level-MPC (OVL-MPC) for the inner loop current control, replacing the classical inner loop proportionate-integral (PI) controller. Furthermore, a deadbeat AC current control is integrated with the OVL-MPC to pursue the modulation of the MMC switches. This means that instead of using switching state-MPC (which is computationally expensive to optimize), OVL-MPC is integrated with the deadbeat AC current control which has a superior transient performance with low computational burden. As a result of a faster convergence of the inner loop OVL-MPC, while the transient performance of the devised controller is much superior to the dual-loop classical PI controller, the steady-state performance is also comparable to the dual-loop classical PI control. This is because the outer loop of the proposed controller is still realized with classical PI control. This complements the nature of the proposed controller with superior transient and robust steady-state performance with the low total harmonic distortion. To enhance system stability, the Moore-Penrose pseudo-inversion is proposed for parameter identification, and a Smith predictor is suggested for delay compensation. Their effectiveness is demonstrated through successful simulation results. Two real-time validation tools i.e., OPAL-RT and RTDS are used separately to verify the performance of the devised controller for different operational power and load transients for both small scale standalone MMC and also high scale MMC integrated in the three terminal HVDC-based power system.

CRediT authorship contribution statement

Milovan Majstorović: Validation, Formal analysis, Conceptualization. Vaibhav Nougain: Writing – review & editing, Writing – original draft, Validation. Leposava Ristić: Writing – review & editing, Supervision. Aleksandra Lekić: Writing – review & editing, Writing – original draft, Supervision, Funding acquisition.

Declaration of competing interest

The authors declare that they have no known competing financial interests or personal relationships that could have appeared to influence the work reported in this paper.

Data availability

No data was used for the research described in the article.

References

- Korn AJ, Winkelnkemper M, Steimer P. Low output frequency operation of the modular multi-level converter. In: 2010 IEEE energy conversion congress and exposition. 2010, p. 3993–7.
- [2] Hiller M, Krug D, Sommer R, Rohner S. A new highly modular medium voltage converter topology for industrial drive applications. In: 2009 13th European conference on power electronics and applications. 2009, p. 1–10.
- [3] Nami A, Liang J, Dijkhuizen F, Demetriades GD. Modular multilevel converters for HVDC applications: Review on converter cells and functionalities. IEEE Trans Power Electron 2015;30(1):18–36.
- [4] Muhammad F, Rasheed H, Spier DW, Prieto-Araujo E, Gomis Bellmunt O. Control design and fault handling performance of MMC for MMC-based DC distribution system. IEEE Access 2022;10:126695–711.
- [5] Lizana R, Perez MA, Arancibia D, Espinoza JR, Rodriguez J. Decoupled current model and control of modular multilevel converters. IEEE Trans Ind Electron 2015;62(9):5382–92.
- [6] Wang J, Tang Y, Lin P, Liu X, Pou J. Deadbeat predictive current control for modular multilevel converters with enhanced steady-state performance and stability. IEEE Trans Power Electron 2020;35(7):6878–94.
- [7] Liu L, Shetgaonkar A, Lekić A. Interoperability of classical and advanced controllers in MMC based MTDC power system. Int J Electr Power Energy Syst 2023;148:108980.
- [8] Jiang C, Zhang S. Power quality compensation strategy of MMC-UPQC based on passive sliding mode control. IEEE Access 2023;11:3662–79.

- [9] Aghahadi M, Piegari L, Lekić A, Shetgaonkar A. Sliding mode control of the MMC-based power system. In: IECON 2022–48th annual conference of the IEEE industrial electronics society. IEEE; 2022, p. 1–6.
- [10] Shi X, Yang R, Cai X, Fang Z, Dong P, Rao F. Improved comprehensive energy-based control for MMC-HVDC system. Int J Electr Power Energy Syst 2023;145:108593.
- [11] Janbazi Ghadi R, Mehrasa M, Ebrahim Adabi M, Bacha S. Lyapunov theory-based control strategy for multi-terminal MMC-HVDC systems. Int J Electr Power & Energy Syst 2021;129:106778.
- [12] Beheshti N, Rezanejad M, Mehrasa M. Linearized control technique with Lyapunov function-based compensators for MMC-based HVDC system under load variation and fault condition. Int J Electr Power Energy Syst 2021;124:106333.
- [13] Liu L, Lekić A, Popov M. Robust adaptive back-stepping control approach using quadratic lyapunov functions for mmc-based hvdc digital twins. In: International symposium on leveraging applications of formal methods. Springer; 2022, p. 126–38
- [14] Ma W, Gong D, Guan Z, Li W, Meng F, Liu X, Wang Y. Compensatory model predictive current control for modular multilevel converter with reduced computational complexity. IEEE Access 2022;10:106859–72.
- [15] Zhang W, Zhang J, Wang Q, Jiang Y, Tan G. Dual-vector model predictive control for modular multilevel converter with low calculation burden. IEEE Access 2024;12:28520–30.
- [16] Shetgaonkar A, Lekić A, Rueda Torres JL, Palensky P. Microsecond enhanced indirect model predictive control for dynamic power management in MMC units. Energies 2021;14(11):3318.
- [17] Dekka A, Wu B, Yaramasu V, Fuentes RL, Zargari NR. Model predictive control of high-power modular multilevel converters—An overview. IEEE J Emerg Sel Top Power Electron 2019;7(1):168–83.
- [18] Cortes P, Kazmierkowski MP, Kennel RM, Quevedo DE, Rodriguez J. Predictive control in power electronics and drives. IEEE Trans Ind Electron 2008;55(12):4312–24.
- [19] Feng Z, Peña-Alzola R, Syed MH, Norman PJ, Burt GM. Adaptive smith predictor for enhanced stability of power hardware-in-the-loop setups. IEEE Trans Ind Electron 2023;70(10):10204–14.
- [20] Feng Z, Peña-Alzola R, Seisopoulos P, Guillo-Sansano E, Syed M, Norman P, Burt G. A scheme to improve the stability and accuracy of power hardware-in-the-loop simulation. In: IECON 2020 the 46th annual conference of the IEEE industrial electronics society. 2020, p. 5027–32.
- [21] Vukosavic SN, Stankovic AM. Non-intrusive estimation of single-port thevenin equivalents in AC grids. IEEE Trans Power Deliv 2021;36(5):2794–803.

- [22] Liao Y, Li Y, Chen M, Nordström L, Wang X, Mittal P, Poor HV. Neural network design for impedance modeling of power electronic systems based on latent features. IEEE Trans Neural Netw Learn Syst 2024;35(5):5968–80.
- [23] Wang S, Dragicevic T, Gao Y, Teodorescu R. Neural network based model predictive controllers for modular multilevel converters. IEEE Trans Energy Convers 2021;36(2):1562–71.
- [24] Liu X, Qiu L, Fang Y, Wang K, Li Y, Rodríguez J. Predictive control of voltage source inverter: An online reinforcement learning solution. IEEE Trans Ind Electron 2024;71(7):6591–600.
- [25] Liu X, Qiu L, Fang Y, Wang K, Li Y, Rodríguez J. Finite control-set learning predictive control for power converters. IEEE Trans Ind Electron 2024;71(7):8190-6.
- [26] Xi-mei L, Qun Z, Qian Z, Zhi-qing Y. Research on deadbeat control strategy of modular multilevel converter. In: Proceedings 2011 international conference on transportation, mechanical, and electrical engineering. TMEE, 2011, p. 621–4.
- [27] Wang C, Ooi BT. Protecting modular multilevel converters (MMC) against ac fault by deadbeat control. In: 2013 IEEE PES Asia-Pacific power and energy engineering conference. APPEEC, 2013, p. 1–6.
- [28] Wang J, Tang Y, Qi Y, Lin P, Zhang Z. A unified startup strategy for modular multilevel converters with deadbeat predictive current control. IEEE Trans Ind Electron 2021;68(8):6401–11.
- [29] Chakraborty R, Gajare PM, Chaki R, Dey A. A simplified dual-stage model predictive controller for modular multilevel converters. Electr Power Syst Res 2023;223:109525, URL https://www.sciencedirect.com/science/article/pii/ S0378779623004145.
- [30] Shetgaonkar A, Karmokar T, Popov M, Lekić A. Enhanced real-time multiterminal HVDC power system benchmark models with performance evaluation strategies. CIGRE Sci Eng 2024;32:1–29.
- [31] Marchand J, Shetgaonkar A, Rueda Torres JL, Lekic A, Palensky P. EMT realtime simulation model of a 2 GW offshore renewable energy hub integrating electrolysers. Energies 2021;14(24).
- [32] Lekić A, Beerten J. Generalized multiport representation of power systems using abcd parameters for harmonic stability analysis. Electr Power Syst Res 2020;189:106658.
- [33] Liu Z, Yang X, Lv X, Chen B, Zhang Y. Dynamic interaction analysis among different control loops and stability enhancement strategy for MMC-HVDC systems. Int J Electr Power Energy Syst 2023;147:108835.
- [34] Chen X, Liu J, Song S, Ouyang S. Circulating harmonic currents suppression of level-increased NLM based modular multilevel converter with deadbeat control. IEEE Trans Power Electron 2020;35(11):11418–29.